ISSN 1990-7931, Russian Journal of Physical Chemistry B, 2024, Vol. 18, No. 1, pp. 308–324. © Pleiades Publishing, Ltd., 2024.

CHEMICAL PHYSICS OF NANOMATERIALS

Experimental and Theoretical Studies of ZnO Nanotubes: an Approach to Chemical Physics Characterization of ZnONTs, Including Morphology, Piezoelectric, and Density of States

M. Monajjemi[a, *], S. Mohammadi[a], S. Shahriari[b], and F. Mollaamin[c]

[a] *Department of Chemical Engineering, Central Tehran Branch, Islamic Azad University, Tehran, 1477893855 Iran*

[b] *Department of Chemistry, Central Tehran Branch, Islamic Azad University, Tehran, 1477893855 Iran*

[c] *Department of Biology, Faculty of Science, Kastamonu University, Kastamonu, 37100 Turkey*

**e-mail: maj.monajjemi@iauctb.ac.ir*

Received September 23, 2023; revised October 17, 2023; accepted October 20, 2023

Abstract—An experimental and theoretical study of the growth of hexagonal ZnO nanotube arrays using a sol gel method and also quantume mechanics and molecular mechanices QM/MM simulation was done by this work. The detailed results of the observed electric output from the calculated piezoelectric potential in the nanotube agrees with that had previously been discussed for nanowires were confirmed. Moreover, double-walled zinc oxide nanotube was used for a theoretic study of a cylindrical molecular capacitor, including an inner cylinder with a positive charge distribution and an outer cylinder with a negative charge distribution based on the experimental fabrication of ZnONTs. Although the SWZnONTs@SWZnONTs behave like Nano cylindrical capacitors, it has been shown in this study that they are not sensitive electrical storage devices compared to SWCNTs. On the other hand using a dopant such as GaN in the DWZnONTs as GaN-DWZnONTs exhibited significant enhancement in the capacitance of these types of capacitors.

Keywords: zinc oxide nanotube, cylindrical molecular capacitor, gallium nitride, piezoelectric potential, hexagonal ZnO proprties

DOI: 10.1134/S1990793124010342

1. INTRODUCTION

1.1. Morphologies of ZnO Nanostructures

Energy shortage and global warming are two important challenges to human beings in the world. Ion batteries, capacitors, solar cells, thermoelectric and piezoelectric technologies have drawn increasing attention due to their potential for converting photon, chemical, thermal and mechanical energies into electrical energy [1–3]. Since one-dimensional nanostructures of ZnO are very important as semiconductors, several morphologies of ZnO nanostructures, such as nanowire [4], nanorods [5], nanobelts [6, 7] and nanotubes [8] have been synthesized using sol gel methods. Zinc Oxide nanotubes have been widely studied and are the center of attention due to their remarkable and outstanding properties such as wide direct band gap and large excited binding energy [9, 10]. This oxide semiconductor has shown promising potential in various applications [11–26], in the field of optoelectronics [27, 28], nanomechanics [29, 30], nanosensors [31–37], resonators [38], electric nanogenerator [39] as well as nanolasers [40]. In additon various methods have been used for their growth [41–43] (Fig. 1).

There are a few different approaches which have been reported for the synthesis of zinc oxide tubular structures. As instance, solution synthesis that normally consist of two-step process. In other words solid forms of one-dimensional zinc oxide are first formed and tubular structures are then obtained by dissolution of materials from the axial part of the solid structures. Fulati and coworkers have reported [44] the fabrication of zinc oxide nanotube pH sensor by a two-step method through low-temperature aqueous chemical growth (ACG). In their method the well aligned zinc oxide Nano-rods have been used followed by the etching to get the SWZnONTs and its comparison to a ZnO nanorod pH sensor. Their results show a linear response of the electrochemical potential of the developed pH sensor to various pH values and twice as high as the sensitivity of the ZnO nanorod pH sensor. One of the important approaches requires a template, in which the zinc oxide is first formed on the external surfaces of the metallic zinc nanowires or Nano-rods, while the removal of metallic cores into the vapor

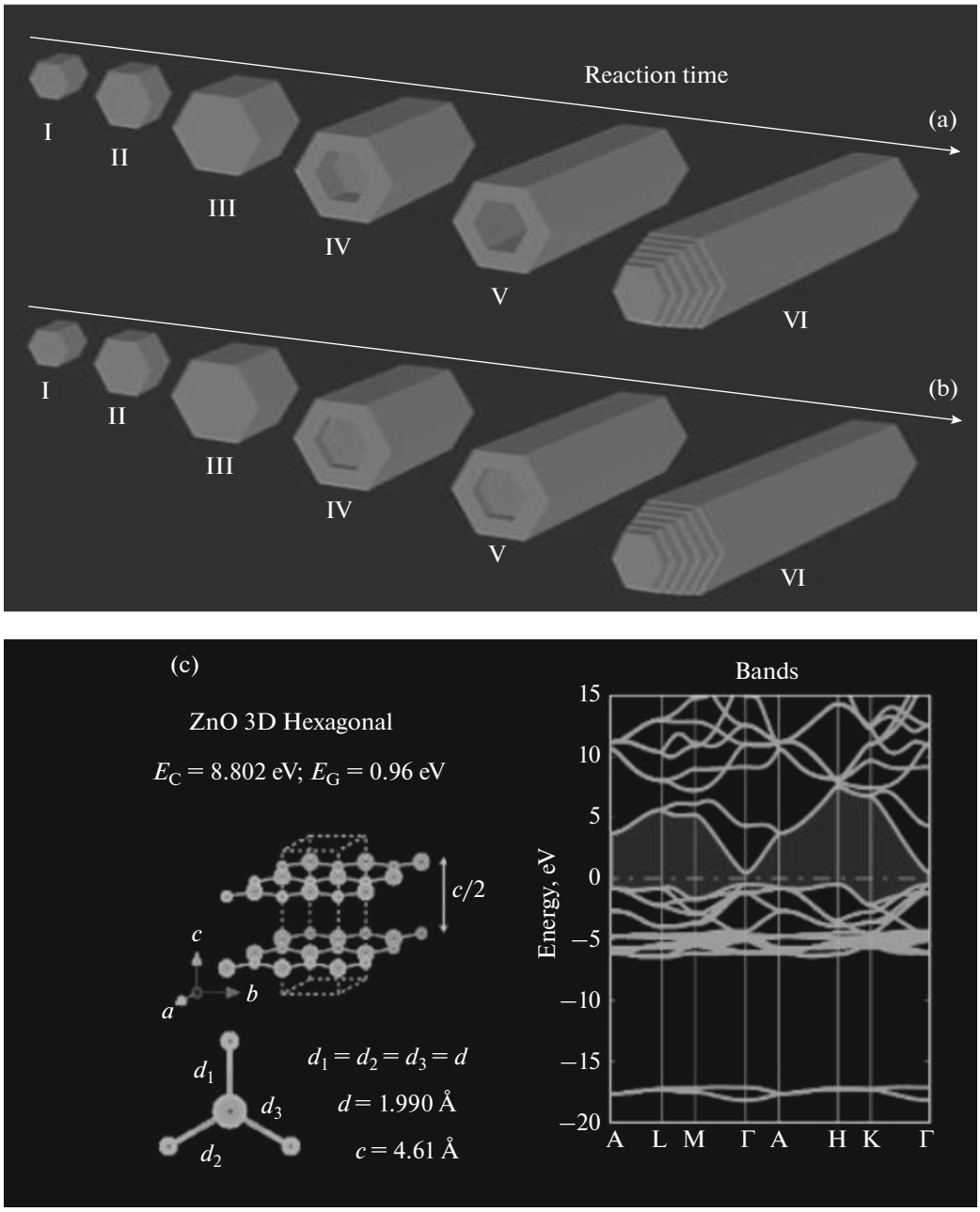

Fig. 1. Schematic structures of the formation of (a) ZnO nanotubes, and (b) ZnO nano rods, (c) crystals of bulk ZnO.

phase at elevated temperatures subsequently gives rise to tubular structures. There is a unique strategy involving vapor phase reactions that can be carried out with PLD (pulsed laser deposition), CVD (chemical vapor deposition) and MOCVD (metal organic chemical vapor deposition), by which open ended SWZnONTs can be prepared directly or indirectly. Using GaN, Y. Xi and coworkers [7] exhibited that (0001) GaN thin film grown on sapphire surfaces can be chosen as the substrate for growing ZnO nanotubes. They showed the close lattice match and structure match between GaN and ZnO could allow a good control over the orientation of the ZnO nanotubes [45]. Generally speaking, in the abovementioned synthesis, the wet systems are more attractive compared to the dry ones due to their ability to produce high quality mono-crystalline ZnO micro- and nanotubes at low cost, promising a large-scale production of novel ZnO materials. Apart from the indirect creation of interior spaces via selective dissolution for SWZnONTs as reported earlier, the search for other more recent methods such as preparation of single crystal SWZnONTs through direct crys-

tal growth in solution, (i. e., similar to those grown in the vapor phase represents a new way in this field of research in producing the DWZnONTs. Therefore, and it should be further investigated for Nano electrical storage such as Nano-capacitor. On the other hand, the direct growth method leads to formation of enclosed DWZnONTs with uniform diameters for that purpose. ZnO nanotubes possess a large band gap (3.4–4 eV) irrespective of the number of walls, diameters, electronic properties and chirality. In addition, they are so stable in terms of chemical and mechanical structures [29, 30]. Therefore, thin single-wall ZnO-NT nanotubes can widely be used as an ideal nanotube for nanoscience to produce special materials such as atomic wires, capacitors and semiconductors [39]. ZnO is a typical semi conductive and piezoelectric material with applications in electronics, optoelectronics, sensors, and energy conversions [46–48]. One-dimensional nanostructures of ZnO are very important semiconductor building blocks with unique and novel physical and chemical properties. As for energy harvesting, ZnO nanowire (NW) array based piezoelectric nanogenerators have been demonstrated to convert mechanical energy into electricity by utilizing the coupled semiconducting and piezoelectric properties of ZnO [49]. The DWZnONTs are suitable materials to produce Nano-cylindrical capacitors. So in this study, we have simulated our systems based on the various distribution diameters of SWZnONTs from the experimental results. This would provide some answers to a few questions regarding the mechanism of the radial charge distribution on the inner and outer electrodes, the band gape, potential difference between two cylinder of the Nano capacitor and finally the capacitance of our system when the inner tube is semiconducting as well as metallic. Therefore, we have studied the SWZnONTs@SWZnONTs including (3,3)@(7,7), (4,4)@(9,9), (4,4)@(11,11), (5,5)@(10,10) and (5,5)@(12,12). And SWZnONTs@GaN-doped-SWZnONT including (3,3)@(7,7) with five molecules of GaN as the dopant, which they can be either p or n type doped. The effects of these doping on the electrostatic properties of the inner and outer tubes can also be calculated for further comparisons and discussions.

1.2. Theoretical Background

Our system is similar to narrow seamless graphitic carbon nanotube cylinders, showing an unusual combination of a nanometer-size diameter and millimeter-size length. This topology, combined with the absence of defects on a macroscopic scale, gives rise to uncommon electronic properties of individual single-wall nanotubes [50] which can be metallic, semiconducting or insulating, depending on their diameter and chirality. Consider a cylindrical capacitor of length "d_l", inner radius "R_{inn}", outer radius "R_{out}", and with charge $Q = d_l q_\lambda$ which q_λ is the charge per unit length (magnitude) on each cylinder (Scheme 1).

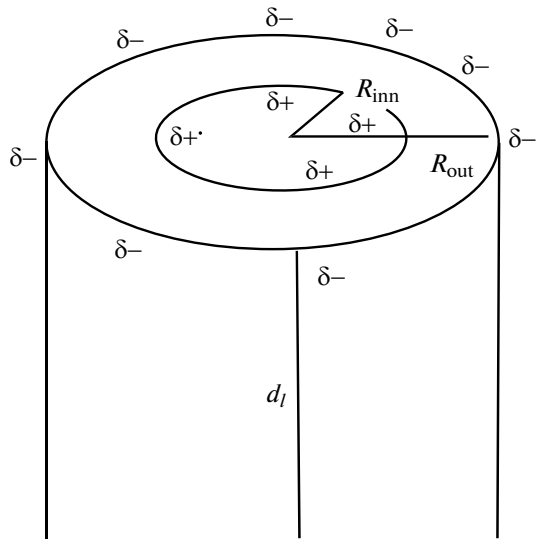

Scheme 1. A schematic of double nanotube as a capacitor including internal and external charges

Assume "d_l" ⩾ "R_{inn}" or "R_{out}" and Neglect fringing and electric field between cylinders, Gauss' law:

$$E(2\pi r d_l) = \frac{d_l q_\lambda}{\varepsilon_0} \Rightarrow E(r) = \frac{q_\lambda}{2\pi\varepsilon_0 r}. \quad (1)$$

In addition, electric potential between cylinders can be written as follows:

$$V_{\text{out}} = 0 \Rightarrow V(r) = -\int_{R_{\text{out}}}^{r} E(r)\,dr$$
$$= -\frac{q_\lambda}{2\pi\varepsilon_0}\int_{o}^{r}\frac{dr}{r} = -\frac{q_\lambda}{2\pi\varepsilon_0}\ln\frac{r}{R_{\text{out}}}. \quad (2)$$

Consequently it can be written as follows

$$V = V_+ - V_- = V_{(\text{inn})} - V_{(\text{out})} = \frac{Q}{2\pi\varepsilon_0 L}\ln\frac{R_{\text{inn}}}{R_{\text{out}}}. \quad (3)$$

According to Eqs. (2) an (3), capacitance for cylindrical geometry can be written as follows

$$\bar{C}_g \equiv Q/V = \frac{2\pi\varepsilon_0 d_l}{\ln(R_{\text{inn}}/R_{\text{out}})}\frac{d_l}{2K\ln(R_{\text{inn}}/R_{\text{out}})}, \quad (4)$$

where K is the dielectric constant of the system. It is notable, $\Delta V_{(\text{inn–out})}$, has a positive amount due to the $2K\ln(R_{\text{inn}}/R_{\text{out}})$, which is positive. This is because the outer layer is at a higher potential than the inner layer. In our system the calculation of the nano-cylindrical capacitors can be obtained from the electrical potential $\emptyset(r, Z)$ in the space between two coaxial cylinders of radii R_{inn} and R_{out} and finite length d_l in the z direc-

tion ($0 \le z \le d_l$). We assumed that the geometrical capacitance in our system is a function of $d_l, R_{\text{inn}}\ R_{\text{out}}$ or $C_g = F(d_l, R_{\text{inn}}, R_{\text{out}})$.

Bilalbegovi [51–53] with a molecular dynamic simulation (for double walled structures of the gold nano-wire) and extension series based on Bessel functions [54] has modified and discussed that capacitance around the shorter coaxial cylinders of radios. Therefore, the capacitance in our model can be calculated via

$$C_g = 2\pi R_{\text{inn}}\varepsilon_0 / V \int_0^{d_l} (\partial\emptyset/\partial r)_{r=R_{inn}} dz, \quad (5)$$

in a finite nanometer-scale cylindrical capacitor (based on the classical electrodynamics). However, on very small scales the quantum corrections will be appearing. It is known that typical inhomogeneous electric fields used in the polarizability measurements for metallic clusters are in the order of 10^5 V cm^{-1} and field gradients are approximately 10^5 V cm^{-2} [55]. These fields induce a dipole moment and slightly deformed clusters. Therefore, to strictly preserve the shape of a nanometer-scale capacitor, weaker and homogeneous fields should be applied in electronic devices.

To calculate the capacitance in Eqs. 4 and 5 for (C_g, C_g), the potential difference applied between two cylindrical plates $V = V_{(\text{inn})} - V_{(\text{out})}$ has been calculated by pop = chelpG command. One of the main purposes of this study in explaining the capacitor model concerns the interaction between SWZnONTs and GaN doped SWZnONTs to be both of electronic transport properties and energy analysis. Although there are many data and a novel methods for electronic transport reports of the double-wall carbon nanotubes [56], no significant studies have been carried out for SWZnONTs@SWZnONTs, highlighting the novelty of this study especially for SWZnONTs@GaN-doped-SWZnONTs model. Using Density-of-states (DOS), we have presented the number of states in unit energy interval, since energy levels are contiguous, Thus, DOS has plotted as curve map. Since our system is isolated, the energy levels are discrete. We have considered the DOS graph as a tool for analyzing the nature of electronic structure in the nanotube. The original total DOS (TDOS) of our system have been calculated based on

$$G(X) = 1/c\sqrt{2\pi}\exp\left(-\frac{x^2}{2c^2}\right), \quad (6)$$

where $c = \dfrac{\text{FWHM}}{2\sqrt{2\ln 2}}$ where the FWHM stands for "full width at half maximum", an adjustable parameter in multi-wave function program where the larger FWHM results in a smoother looking TDOS graph look smoother and, making the analysis to be performed easier. The normalized Lorentzian function ($L(x)$) is defined as

$$L(x) = \text{FWHM}/2\pi(x^2 + 0.25\text{FWHM}^2). \quad (7)$$

Pseudo-Voigt function is weighted as linear combination of Gaussian function and Lorentzian function [57–59]:

$$P(x) = w_{\text{gauss}}G(x) + (1 - w_{\text{gauss}})L(x). \quad (8)$$

2. METHODOLOGY

2.1. Experimental

In our experiments, (0001) GaN thin film grown on sapphire surfaces was chosen as the substrate for growing ZnO nanotubes. The close lattice match and structure match between GaN and ZnO allow a good control over the orientation of the ZnO nanotubes. GaN substrate was cleaned by a standard cleaning process. First, GaN substrate was ultrasonicated consecutively in acetone, ethanol, IPA (isopropyl alcohol), and de-ionized water for 5 min, respectively; then it was blown dry with nitrogen gas to eliminate any adsorbed moisture. The next step was to prepare the nutrient solution. The nutrient solution was composed of a 1 : 1 ratio of zinc nitrate to hexa-methylene-tetramine (HMTA). Both of the chemicals were reagent grade from Fluka (St. Louis, MO). The substrate was put face down at the top of the nutrient solution surface. The reaction vessel was heated to 95°C and kept at 95°C for 2–3 h and then heated to 50°C and kept at 50°C for 3–48 h, and finally was allowed to cool down naturally. The current synthesis route has manifested the unique advantage of being without any post-treatment or any surfactant. The products were examined using a LEO 1530 scanning electron microscope (SEM) (Figs. 2, 3).

2.2. Computational Details

Calculations were performed using GAMESS-US packages [60]. In this study, we have mainly focused on getting the optimized results for each tube from DFT methods including the m06 and m06-L. The m062x, m06-L, and m06-HF are a novel Meta hybrid DFT functional with a good correspondence in non-bonded calculations and are useful for calculating the energies of the distance between two coaxial cylinders of radii R_{inn} and R_{out} in the cylindrical capacitor [61]. Pm6 including pseudo=lanl2 calculations using gauessian program have been carried out done for the non-bonded interaction between DWZnONTs. M06 and m06-L (DFT) functional are based on an iterative solution of the Kohn-Sham equation [62] of the density functional theory in a plane-wave set with the projector-augmented wave pseudo-potentials. The Per-

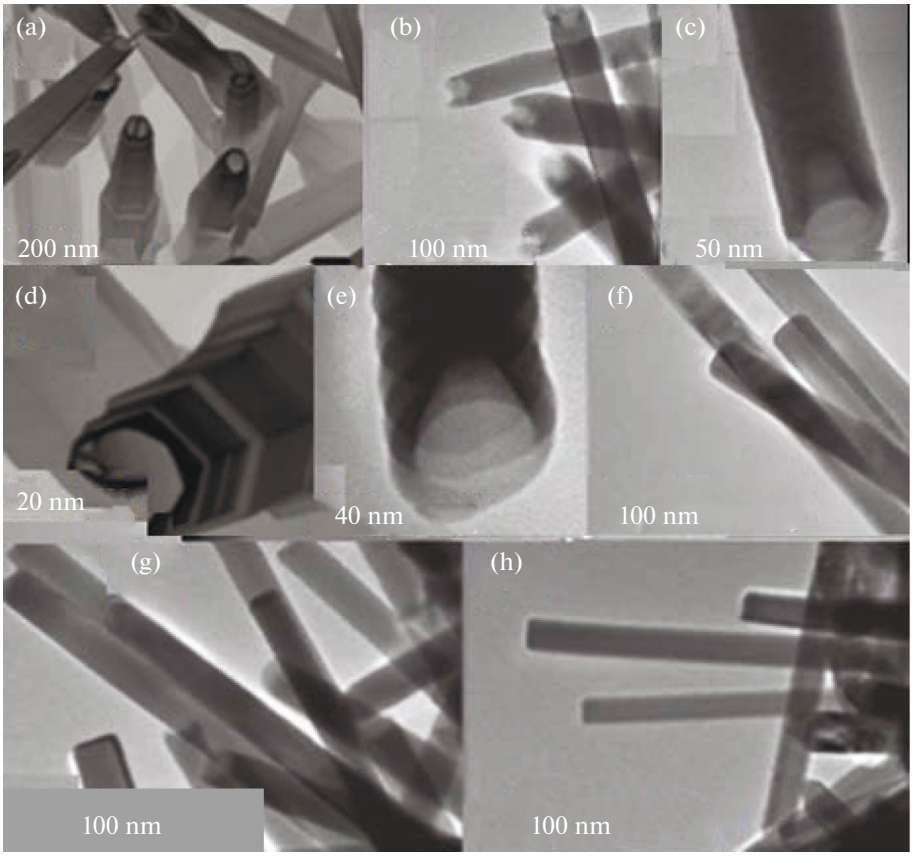

Fig. 2. TEM images of the 50 nm ZnO Nano rods: (a), (b) panoramic views; (c)–(e) detailed views of the concave growing heads of ZnO Nano rods, where growth oscillation (ring-like marks) is also apparent; (f)–(h) flat (000–1) ends of the ZnO nanorods.

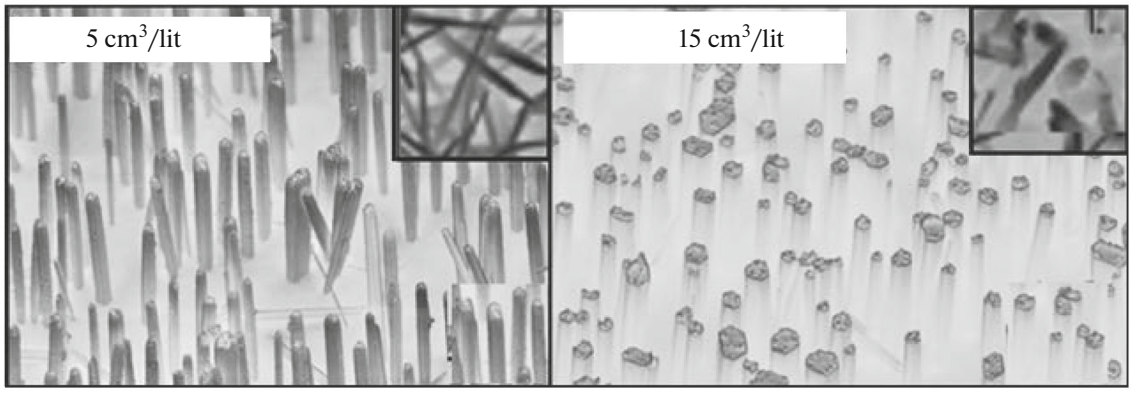

Fig. 3. A series of SEM images of ZnO nanotube arrays grown first at 95°C for 3 h and then at 50°C for 16 h with a solution concentration of (a) 5, (b) 15 h.

dew–Burke–Ernzerhof (PBE) [63] exchange-correlation (XC) functional of the generalized gradient approximation (GGA) has been also used. The optimizations of the lattice constants and the atomic coordinates are made by the minimization of the total energy. A fixed SWZnONTs geometry with Zn–O bond lengths of 1.895 Å is chosen with no further geometry optimization. The outer ring, initially placed at the center of the inner tube, is rigidly axially been shifted and rotated around the fixed inner shell. At each inter-tube configuration, a single-point calculation is carried out and the total energy is recorded. The resulting sliding-rotation energy surfaces are used to fix our model in better position. We employed density

functional theory with the van der Waals density functional to model the exchange-correlation energies of SWZnONTs [64]. The double ζ-basis set with polarization orbitals (DZP) were used for SWZnONTs. For non-covalent interactions, the B3LYP method is unable to describe van der Waals [65] capacitor systems by medium-range interactions such as the interactions of two cylinders. The B3LYP and most other functional are rather insufficient to illustrate the exchange and correlation energy for distant non-bonded medium-range systems. Moreover, some recent studies have shown that inaccuracy for the medium-range exchange energies leads to large systematic errors in the prediction of molecular properties [66, 67]. We further calculated the interaction energy between two coaxial cylinders of radii R_{inn} and R_{out} for each SWZnONTs in our structures (The number of nanotubes was varied to examine size-dependent electrical properties). The dielectric permittivity as a function of dielectric size was determined using abinito calculations. The interaction energy for capacitor was calculated via an Mp6 method in all items based on the Eq. (9):

$$\Delta E_S\,(\mathrm{eV}) = E_{total} - \left(E_{SWZnONT(inn)} + \mathrm{E}_{SWZnONT(out)}\right) + E_{BSSE}, \quad (9)$$

where ΔE_S is the minimum energy of capacitor. The charge transfer and electrostatic potential-derived charges were also calculated using the Merz–Kollman–Singh [68], chelp [69], and chelpG [70]. The charge calculation methods based on molecular electrostatic potential (MESP) fitting are not well-suited for treating larger systems whereas some of the innermost atoms are located far away from the points at which the MESP is computed. In such conditions, variations of the innermost atomic charges would not lead towards a significant change of the MESP outside of the molecule. This approach (CHELPG) is shown to be considerably less dependent upon molecular orientation than the original CHELP program. The results are compared to those obtained by using CHELP. In the CHELPG (Charges from Electrostatic Potentials using a Grid based method), atomic charges are fitted to reproduce the molecular electrostatic potential (MESP at a number of points around the molecule). The MESP is calculated at a number of grid points spaced 3.0 pm apart and distributed regularly in a cube. Charges derived in this way don't necessarily reproduce the dipole moment of the molecule. CHELPG charges are frequently considered superior to Mulliken charges due to their lower dependency on the underlying theoretical method used to compute the wave function (and thus the MESP). The representative atomic charges for molecules should be computed as average values over several molecular conformations. A detailed overview of the effects of the basis set and the Hamiltonian on the charge distribution can be found in previous studies [71–74]. We have also extracted the charge density profiles from the first principle calculations through an averaging process described [75]. We have calculated the electron density (Both of Gradient norm and Laplacian), value of orbital wave-function, electron spin density, electrostatic potential from nuclear/atomic charges, electron localization function (ELF), localized orbital locator (LOL defined by Becke and Tsirelson), total electrostatic potential (ESP), as well as the exchange-correlation density, correlation hole and correlation factor, and the average local ionization energy using the multifunctional wave-function analyzer [57–59]. The contour line map has drawn via Multiwfn software [58, 59]. The solid lines indicate positive regions, while the dash lines indicate negative regions. We have plotted the contour line corresponding to vdW surface (electron density = 0.001 a.u., which is defined by R.F.W. Bader). This is useful to analyze distribution of electrostatic potential on vdW surface. Such a contour line has also been plotted in gradient line and vector field map by the same option. Color, label size and line style of the contour line can be changed based on models. The relief map has used to present the height value at every point. If values are too large, they will be truncated in the graph. Therefore, it can be chosen to scale the data with a factor to avoid truncation. The graph is shown on interactive interface. Shaded surface map and shaded surface map with projection are used in our representation of height value at each situation [57–59].

3. RESULTS

3.1. Experimental Results

Figure 1, describes schematically the two growth processes for the formation of the nanotubes and nanorods of ZnO in present study. In route (a), a single crystal nucleus grows preferentially along its [0001] direction (stages I to III; our current synthetic conditions favor the growth of [0001]). During the related reactions, the nanotubes were grown as; $Zn^{2+} + 2OH^- \leftrightarrow Zn(OH)_2$ and $Zn(OH)_2 \leftrightarrow ZnO + H_2O$ The growth process of the ZnO nanotube arrays could be divided into two stages.

The first growth stage corresponds to the precipitation of ZnO nanorod arrays at a higher temperature (90°C). It is well-known that the hexagonal ZnO crystal has both polar and non-polar faces. The oxygen-terminated (0001) and the zinc-terminated (0001) are the typical polar surfaces. Non-polar faces are more stable than the metastable polar faces. At the early stage of the reaction, the growth units (ZnO_2^{2-}) in the solution near the surface of ZnO nuclei are likely adsorbed on the positive polar faces of the (0001) surface; and a faster growth along the [0001] direction forms nanorods. After an induction period, rapid deposition of product species on the wall rims is

expected, which results in a tubular interior (stage V); note that the six prismatic crystal planes of ZnO are fairly stable in this type of 1-D growth. When the nutrients are further consumed, the growth goes back to normal planar growth of {0001}, leading to an enclosure process for the nanotube, since the {0001} in-plane growth will reduce the opening of the tubular structure. Under lower supersaturation conditions (stage VI; i.e., in Fig. 1), areas of the {0001} planes are becoming smaller and smaller, resulting in a gradual reduction in head diameter. Associated with this process, from stages IV to VI, a growing nanotube head undergoes a shape transformation from a concave structure to a convex tip, that is, we observe an inversion from a "negative volume". In the present work, we first employed a high alkali concentration (molar ratio of $Zn^{2+}/OH^{-} = 1 : 20$ Under these conditions, the 1-D product has diameters in the region of about 50 nm, and the growth essentially follows route (b) of Fig. 1. As displayed in Figs. 2a, 2b, concave growing heads of nanorods along the [0001] direction can be observed in a large proportion of the product. Interestingly, an inward cone-shaped space can be observed in most growing heads of the ZnO nanorods (Figs. 2c–2e), and growth oscillation can also be seen clearly in the ring-like contrasts of these TEM images. Accordingly, flat {000 1} ends of these nanorods can also be seen in an equal quantity. Figure 3 describes schematically the two growth processes for the formation of the nanotubes and Nano rods of ZnO obtained in our study. In route (a), a single crystal nucleus grows preferentially along its [0001] direction (stages I to III; our current synthetic conditions favor the growth of [0001]). At a certain stage (stage IV), the wall rim grows faster than its central base, and a concave growth head is formed along the [0001] direction. When the reaction is accelerated after an induction period, rapid deposition of product species on the wall rims is expected, which results in a tubular interior (stage V); note that the six prismatic crystal planes of ZnO are fairly stable in this type of 1-D growth. When the nutrients are further consumed, the growth goes back to normal planar growth of {0001}, leading to an enclosure process for the nanotube, since the {0001} in-plane growth will reduce the opening of the tubular structure. Under lower super saturation conditions (stage VI; i.e., close to the end of the batch reactions), areas of the {0001} planes are becoming smaller and smaller, resulting in a gradual reduction in head diameter. Associated with this process, from stages IV to VI, a growing nanotube head undergoes a shape transformation from a concave structure to a convex tip, that is, we observe an inversion from a "negative volume" (i.e., hollow space) to a "positive volume" (i.e., solid matter). In contrast to route (a), which creates kinetically an interior space within the 1-D structure, route

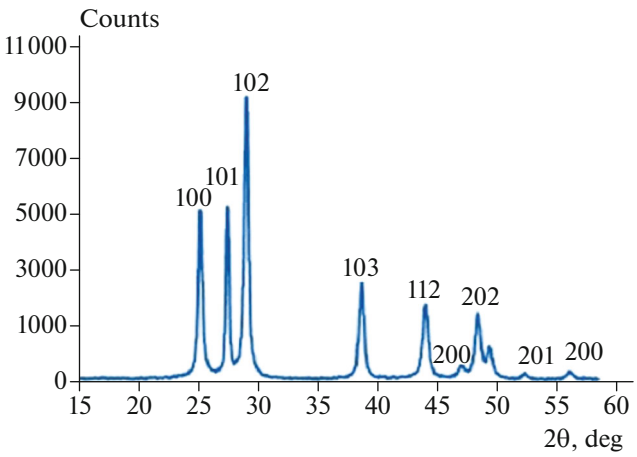

Fig. 4. X-ray diffraction pattern of the as-grown ZnO nanotube arrays on GaN (100) with the ZnO (101) peak rocking curve.

(b) produces a solid Nano rod. Although in stages IV and V, a concave growing head can still be formed, the difference between the wall rim and central base is much smaller. This shallow vacant space can be readily filled up when the growth rate is slowed down, producing the solid Nano rod. In both cases, however, the shapes of growing heads of the 1-D nanostructures undergo the same concave-to convex transformation. The SEM images of the nanotubes grown under different concentrations (5, 15, 20, 25 and 30 mmol/L) but at the same temperature and growth time (95°C (3 h) then 50°C (16 h)) are presented in Fig. 3. Figure 3a indicates that the ZnO nanotube arrays hardly grew when the concentration was 5 mmol/L. The first sight of ZnO nanotube formation was when the concentration reached 15 mmol/L (Fig. 3b). Figure 4 exhibits the representative X-ray diffraction (XRD) spectrum recorded with the incident X-ray normal to the substrate.

3.2. Theoretical Results

For modeling the nanotubes including single walle and multi wale same as Fig. 1, we first consider 3D ZnO tubes in various diameter and chirality which (3,3)@(7,7) structure is found most s compared to (5,5)@(12,12) which is a rather unstable form. The stability depends on the distance between inner radius "R_{inn}", and outer radius "R_{out}" in one side and the chirality in other side Table 1. The minimum energies are calculated based on Eqs. (5), (6) in terms of the total energy of the optimized structures which are listed in Table 1 (Fig. 5). The differences in the band structure and Fermi level energy of different tubes have been calculated. Furthermore, we have presented the number of states in unit energy interval through density of states (DOS). Since the energy levels are

Table 1. The band structure and Fermi level energy of the ZnO@ZnO structure

Nanotube ZnO@ZnO	Atom No.	Fermi energy, kJ/mol	HOMO, a.u.	LUMO, a.u.	Gap energy, kJ/mol	Relative energy, a.u.	$\Delta E_S = E_{total} - (E_{(inn)} + E_{(out)})$	$R_{inn} - R_{out}$, Å
(3,3)@(7,7)	140	−913.5	−0.347953	−0.240903	281.06	−1.9068974	−4.39 eV	3.58
(4,4)@(9,9)	182	−893.3	−0.340244	−0.227983	294.74	−0.8248715	−0.93 eV	4.87
(4,4)@(11,11)	210	−905.6	−0.344945	−0.227262	308.98	0.0000000	+0.25 eV	6.37
(5,5)@(10,10)	210	−901.7	−0.343459	−0.228012	303.15	+0.0579037	−0.69	4.53
(5,5)@(12,12)	238	−850.9	−0.324091	−0.227069	254.72	+0.5226099	+10.00	6.39

contiguous and our system is isolated (the energy levels are discrete), DOS was plotted as a curved map and we have considered those graphs as a tool for analyzing the nature of electronic structure in our systems. The original total DOS (TDOS) of our system was calculated based on Eq. (6) and are shown in Fig. 6 for energies between (−0.8) to (−0.4 a.u.) and Fig. 7 for energies between (−0.3) to (+0.2 a.u.). Charge transfer from Zn atoms to O atoms is a measure of the ion-icity of ZnO in tubular structures. We have calculated the amount of charge on constituent Zn and O atoms in our systems by performing the Mulliken atomic charges and ChelpG analysis. The calculated value of charge transfer for (3,3)@(7,7) from inner to outer tubes is found to be 1.03 electrons which is an acceptable value (Table 1). This amount for other tubes depends on the stability and chirality which is negligible for the (5,5)@(12,12) structures due to their unstable form. This analysis clearly indicates that a significant amount of charge is transferred from inner tubes which are closed to outer tubes. The Zn–O bond, d = 1.895 Å was fixed for the SWZnONTs where the calculated structural parameters are significantly larger than those of SWCNTs and SWBNNTs structures due to fact that Zn has larger radius than that of B, C, N and O atoms. It should be noted that the length of Zn–O bonds of 2D ZnO honeycomb structure is smaller than that in the 3D bulk (wz, zb) crystals, since *sp*2 bonding in the former is stronger than the tetrahedral coordinated *sp*3 bonding in the latter. The interaction between ZnO planes appears to slightly weaken the Zn–O bonds of h-ZnO crystal. As a result the length of the Zn–O bonds becomes larger than that of 2D ZnO honeycomb structure.

4. DISCUSSION

4.1. Electronic Structure Related to DOS Interpretation

The information of the DOS can be further refined by separating—or *projecting*—its contributions from individual atoms or orbitals in the system. The so-called projected density of states (PDOS) is a very useful tool for rationalizing chemical phenomena, since it permits indentifying how the electronic states of some particular specie changes when exposed to different environments. In order to gain some chemical insight from these changes, we have analyzed the PDOS for all ML surface adducts. The results are presented in the next sections, giving a brief discussion on the adsorption geometry in each case. The picture shows important contribution from first oxygen to the valence band maximum (VBM), where the PDOS peak at ~−0.45 a.u. (Fig. 6a) evidences that localized O states still remain on the surface, although shifted slightly down in energy because of the hydrogen bond with the ligand. The PDOS analysis for the Me–OH case leads to identical qualitative conclusions. With comparable adduct geometries, the Me–OH and Me–NH_2 surface adducts lead to very similar changes in the surface's electronic structure (Fig. 8). Both ligands appear to suppress the surface resonances observed for the bare surface, resulting in a DOS apparently free of intra-gap levels (see Fig. 8). This effect is a direct consequence of the hydrogen bonds formed on the surface, as evidenced by the PDOS depicted in the Fig. 6 for the Me–NH_2 case. The picture shows important contribution from O 1st to the valence band maximum (VBM), where the PDOS peak at ~−0.45 eV evidences that localized O states still remain on the surface, although shifted slightly down in energy because of the hydrogen bond with the ligand. The PDOS analysis for the Me–OH case leads to identical qualitative conclusions. Through the PDOS analysis it is also possible to identify the ligand-substrate electronic interaction, with a noticeable component from the N atom spread all along the VB. Nevertheless, the contributions from the Zn(4s) orbitals are insignificant along the VB, indicating that the ligand-substrate interaction does not correspond to a Lewis acid-base adduct in this case. Instead, there is a delocalized interaction with the O network in the oxide, with the same pattern also found for the Me–OH case. Note that such delocalized electronic interactions do not necessarily have a bonding character. In fact, every energy band is always bonding in its lower and anti-bonding in its upper half. Other similarities are the dominance of an anti-bonding character on the sulfur's PDOS distribution and the absence of sig-

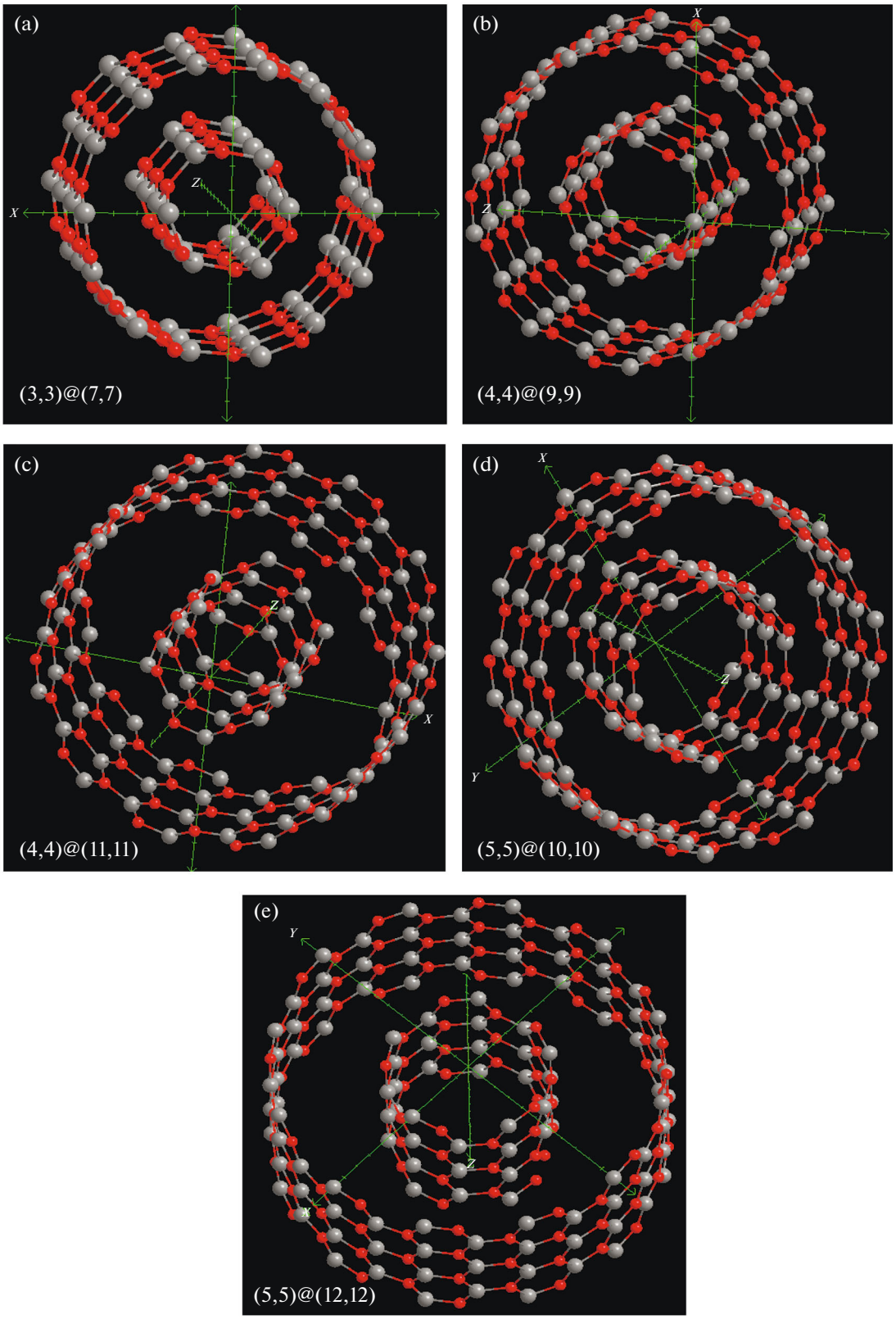

Fig. 5. The optimized structures of SWZnONTs@SWZnONTs, including (a) (3,3)@(7,7), (b) (4,4)@(9,9), (c) (4,4)@(11,11), (d) (5,5)@(10,10), and (e) (5,5)@(12,12).

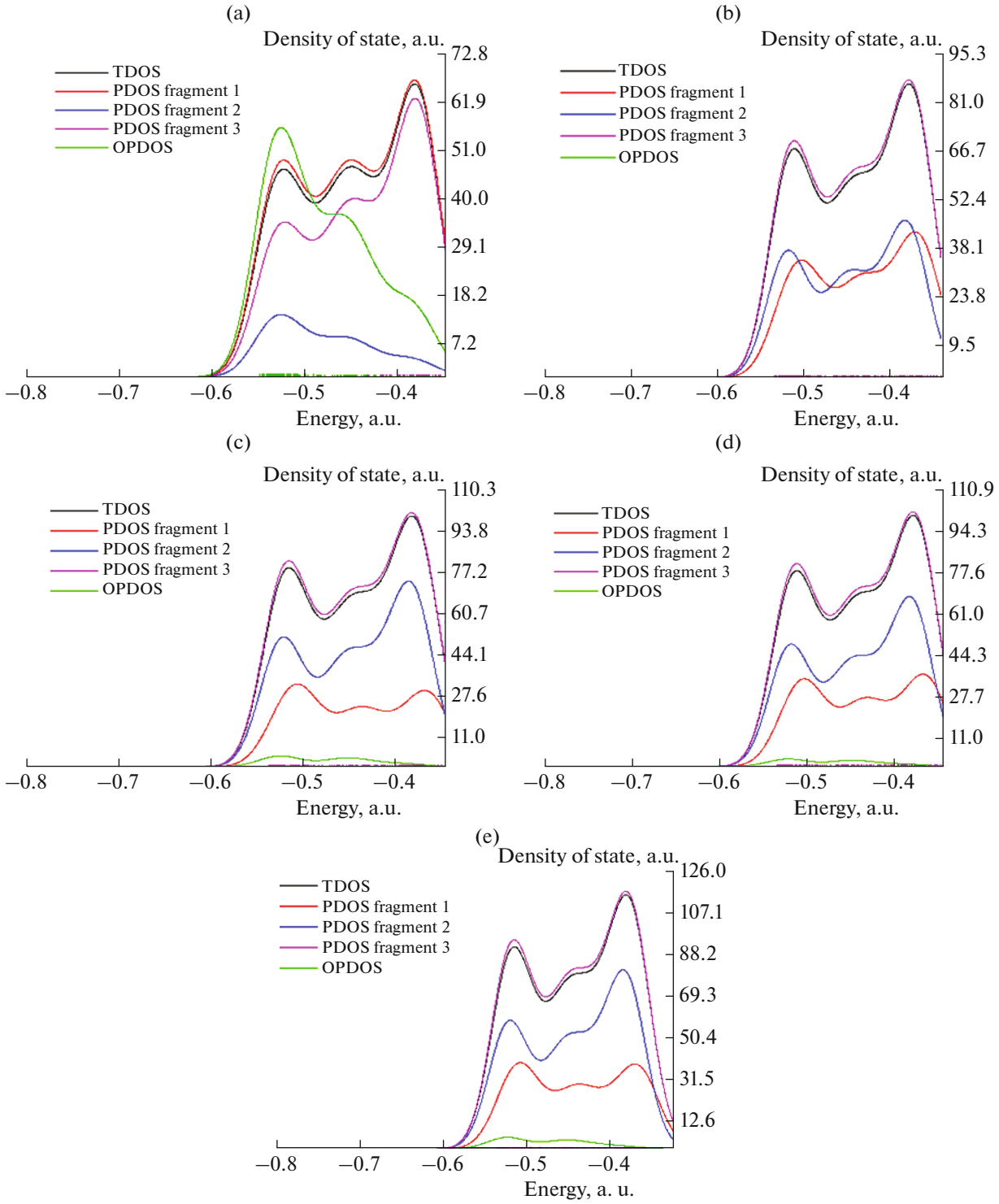

Fig. 6. Total/Partial/Overlap population density-of-states (TDOS, PDOS, OPDOS) based on Eq. (6) for (a) (3,3)@(7,7), (b) (4,4)@(9,9), (c) (4,4)@(11,11), (d) (5,5)@(10,10), and (e) (5,5)@(12,12), between –0.8 to –0.4 energies (a.u).

nificant contributions from Zn(4s) orbitals in the VB. As an apparent difference, a sharp peak between ~ –0.6 up to ~–0.6 eV (Figs. 6b, 6c) occurs, being a signature of the localized Zn–O bond. The covalent interaction with the O network is again expected to play just a marginal role in the adduct stabilization, with no significant evidence of a classical Lewis acid-base adduct. This finding is in fact very consistent with the smooth *EB* changes with the adduct's geometry. For the surface resonance at ~0.2 to –0.8 eV (Figs. 6, 7),

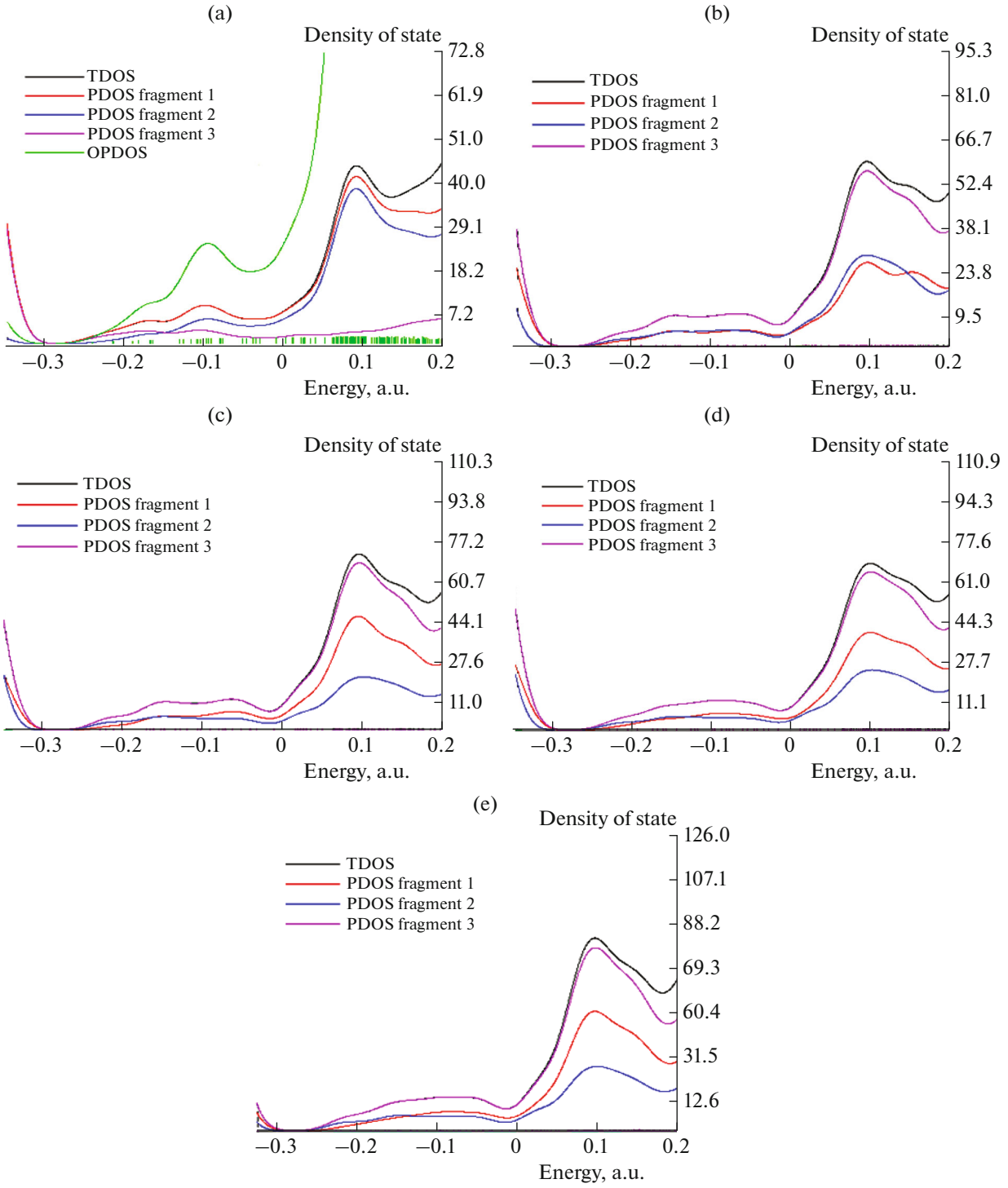

Fig. 7. Total density of states of the system based on Eq. 6 for (a) (3,3)@(7,7), (b) (4,4)@(9,9), (c) (4,4)@(11,11), (d) (5,5)@(10,10), (e) (5,5)@(12,12), between –0.3 to 0.2 energies (a.u).

the signatures of both O1 and O2 are quite similar, while a smaller contribution from the carboxylic carbon atom is perceptible in the same region (not shown). All three components show a shoulder in their TDOS distributions—from ~0.2 to –0.8 eV (Figs. 6, 7), indicating some electronic hybridization with the substrate levels. However, such delocalized contribution decays faster for O2, showing that the ligand-substrate electronic interaction is preferentially mediated through O1. As discussed for the Me–SH case (Fig. 8), such

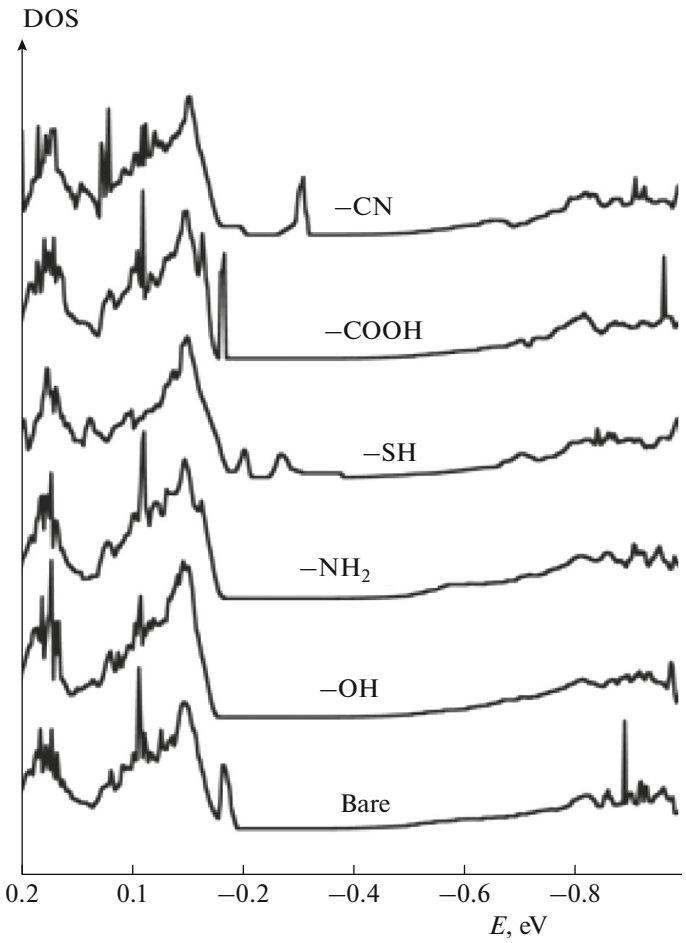

Fig. 8. DOS for the bare and modified ZnO-(1010) surfaces. The origin of the energy axis corresponds to the conduction band minimum in all cases by DFT calculations.

interactions are predominantly anti-bonding and also impose Pauli repulsions to the O network on the substrate. Consequently, electrostatic interactions and the passivation of the surface levels also seem to be the driving forces of the adsorption process in this case.

The different charge and electron density, Gradient norm and Laplacian, electron spin density, electrostatic potential from nuclear/atomic charges, electron localization function (ELF), localized orbital locator and the partial density of states are presented in

Table 2. Calculated $\acute{C}_g$ as well as the diectric based on the geometry of our system for ZnO@ZnO structure

Nanotube ZnO@ZnO	$\acute{C}_g$	$\ln\frac{R_{inn}}{R_{out}}$	k	$\sum_{inn} Q$	$\sum_{out} Q$	$\Delta E_S = E_{total} - (E_{(inn)} + E_{(out)})$	$R_{inn} - R_{out}$, Å
(3,3)@(7,7)	140	–0.82	–0.347953	+1.02	–0.98	–4.39 eV	3.58
(4,4)@(9,9)	182	–0.82	–0.340244	0.74	–0.73	–0.93 eV	4.87
(4,4)@(11,11)	210	–1.01	–0.344945	0.09	–0.09	+0.25 eV	6.37
(5,5)@(10,10)	210	–0.68	–0.343459	0.3	–0.3	–0.69	4.53
(5,5)@(12,12)	238	–0.86	–0.324091	0.01	–0.01	+10.00	6.39

k—Dielectric constant.

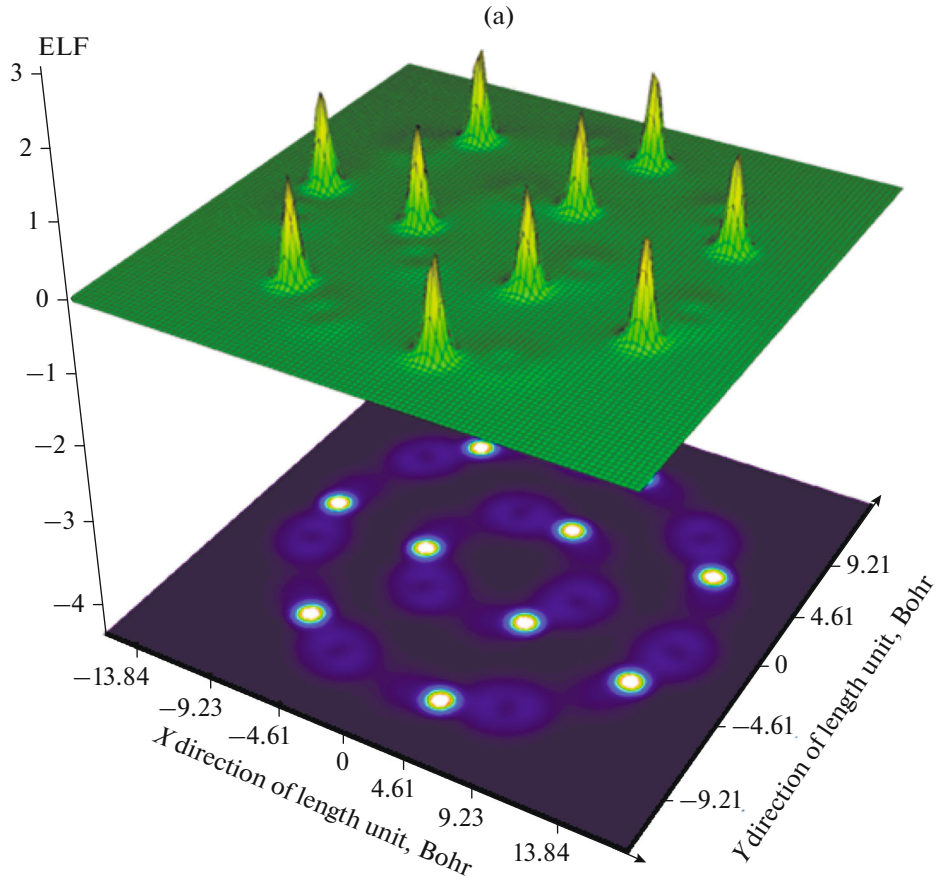

Fig. 9. Electron localization function (ELF), localized orbital locator (LOL) and the partial density of states, (a) ELF without GaN, (b) LOL including GaN, (c) contour plots of total charge, (d) electrostatic situation interaction with GaN.

Fig. 9. Contour plots of total charge indicate high density around O atoms. High density contour plots around O atoms protruding towards the Zn–O bonds indicate charge transfer from Zn to O atoms. This way the Zn–O bond acquires an ionic character. The charge transfer from Zn to O is analyzed by using different schemes of chelp G and Mulliken atomic charges. Table 2 indicates the calculated $\acute{C}_g$ as well as the dielectric based on the geometry of our system. It is shown that despite the fact that the SWZnONTs@SWZnONTs is a cylindrical capacitor, it does not have a sensitive electrical storage compared to SWCNTs@ SWCNTs. However, using a dopant such as GaN in the SWZnONTs@GaN-SWZnONTs can increase its capacitance significantly.

4.2. Hetero-structures of Multiwall ZnO Nanotubes

A high-resolution TEM images of the heterostructure of nanotube and coaxial nanocable as well as the corresponding diffraction patterns are shown in Figs. 2, 3. The images reveal that all of the sheath and the core portions of the nanotube exhibit clear lattice images, indicating well crystallized structures. The thickness of the sheath of nanocable and the doble wall of nanotubes are between 4–8 nm. With the quantitative EDS result, the diffraction pattern of the nanotubes are identified to be the hexagonal ZnO nanotubes shown in Figs. 2, 3. As-grown nanotubes are single crystals and each of which has a growth direction of wurtzite (100) (Fig. 4). The darker contrast on the edge and appearance of lattice image in the central region typically observed in the TEM images of the ZnO nanotube that are consistent with simulation results of quantume mechanics and molecular mechanices (QM/MM) of a multiwall achiral positions including (a) (3,3)@(7,7), (b) (4,4)@(9,9), (c) (4,4)@(11,11), (d) (5,5)@(10,10), and (e) (5,5)@(12,12).

Nanotubes calculated by DFT methods, as shown in Fig. 4. It is composed of two sets of single crystal diffraction patterns with epitaxial relationship. The two sets of diffraction patterns are indexed as the hexagonal ZnO and ZnO/GaN by referring to the quantitative EDS analysis also. Furthermore, the TEM images indicates that all ZnO nanotubes are grown along the proper direction. Therefore, we conclude

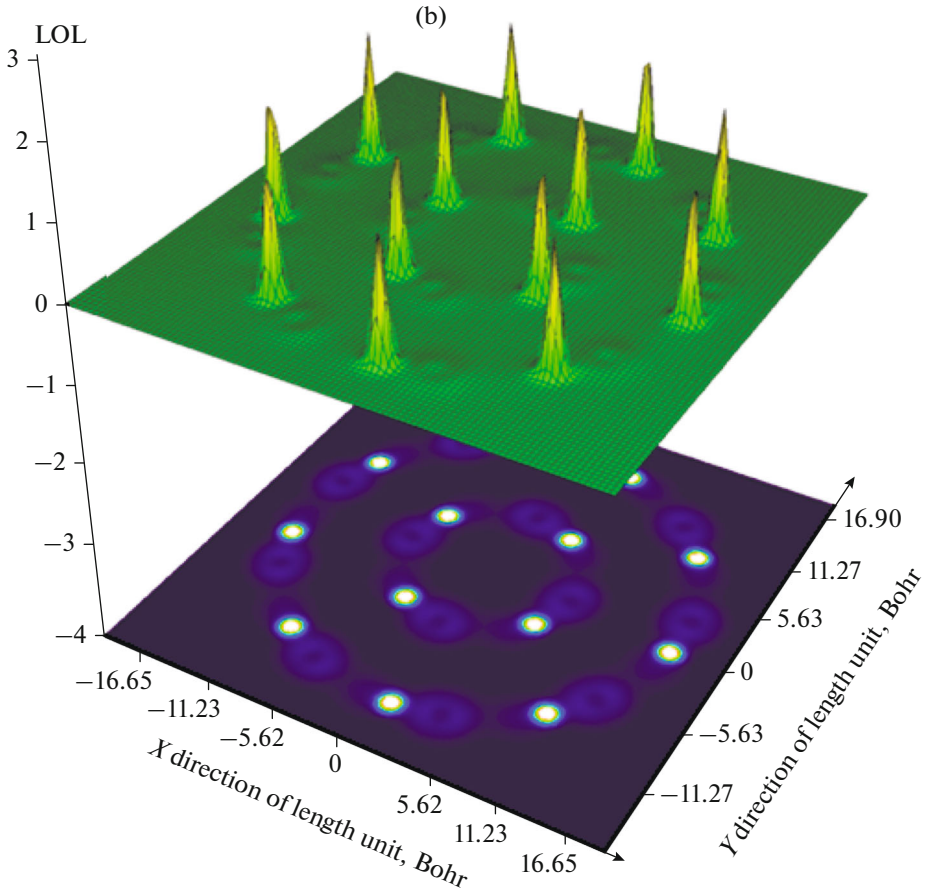

Fig. 9. (Contd.)

that the 1D heterostructures, which are composed of DWCNTs with longitudinal axis along the proper direction, are formed by piezoelectric and DOS proprties.

4.3. Electronic Structure and Diffraction Analysis

This study indicated two monolayer of ZnO grown on GaN substrate using surface X-ray diffraction and scanning tunneling microscopy. We confirmed that the transition to the bulk wz-ZnO structure occurs in several monolayer coverage. The Zn–O bond length of the planar hexagonal structure measured 1.91 Å is slightly larger than the the value of 1.89 Å calculated for the the bond length of the monolayer of ZnO (Fig. 4). This situation implies that the effect of the GaN substrate may be negligible. As shown in the Fig. 4, all of the diffraction peaks match the ZnO structure comparing with theory calculation, with structure of SWZnONTs@SWZnONTs including (3, 3)@(7,7), (4,4)@(9,9), 4, 4)@(11,11), (5,5)@(10,10) and (5,5)@(12,12). And SWZnONTs@GaN-doped-SWZnONT including (3,3)@(7,7) with five molecules of GaN as the dopant. The dominant appearance of the (100), (101) and (102) peaks shows its orientation relationship. The hexagonal shapes of the nanotubes as revealed by the SEM images are consistent with the XRD data (Fig. 4). A weak (201) and (202) peaks of ZnO as observed in XRD spectrum shows that there were some flipped over tubes on the substrates, which were captured by SEM. On the basis of our selectedarea electron diffraction and high-resolution SEM studies, we affirm that the nanotube materials are singlecrystalline and the axial direction is along [102]. Furthermore, similar to the case for the 50 nm ZnO nanorods, our structural and compositional analyses con fi rm that the ZnO nanotubes have an atomic ratio of Zn : O ≈ 1 : 1, and they are indeed in the wurtzite phase.

CONCLUSIONS

Hexagonal ZnO nanotube arrays were synthesized by a low temperature solution chemical method. The morphologies of the ZnO nanotube arrays were studied under different growth conditions, such as the growth time, the growth temperature and the concentration of the nutrient solution. Piezoelectric nanogenerators using ZnO nanotube arrays were demon-

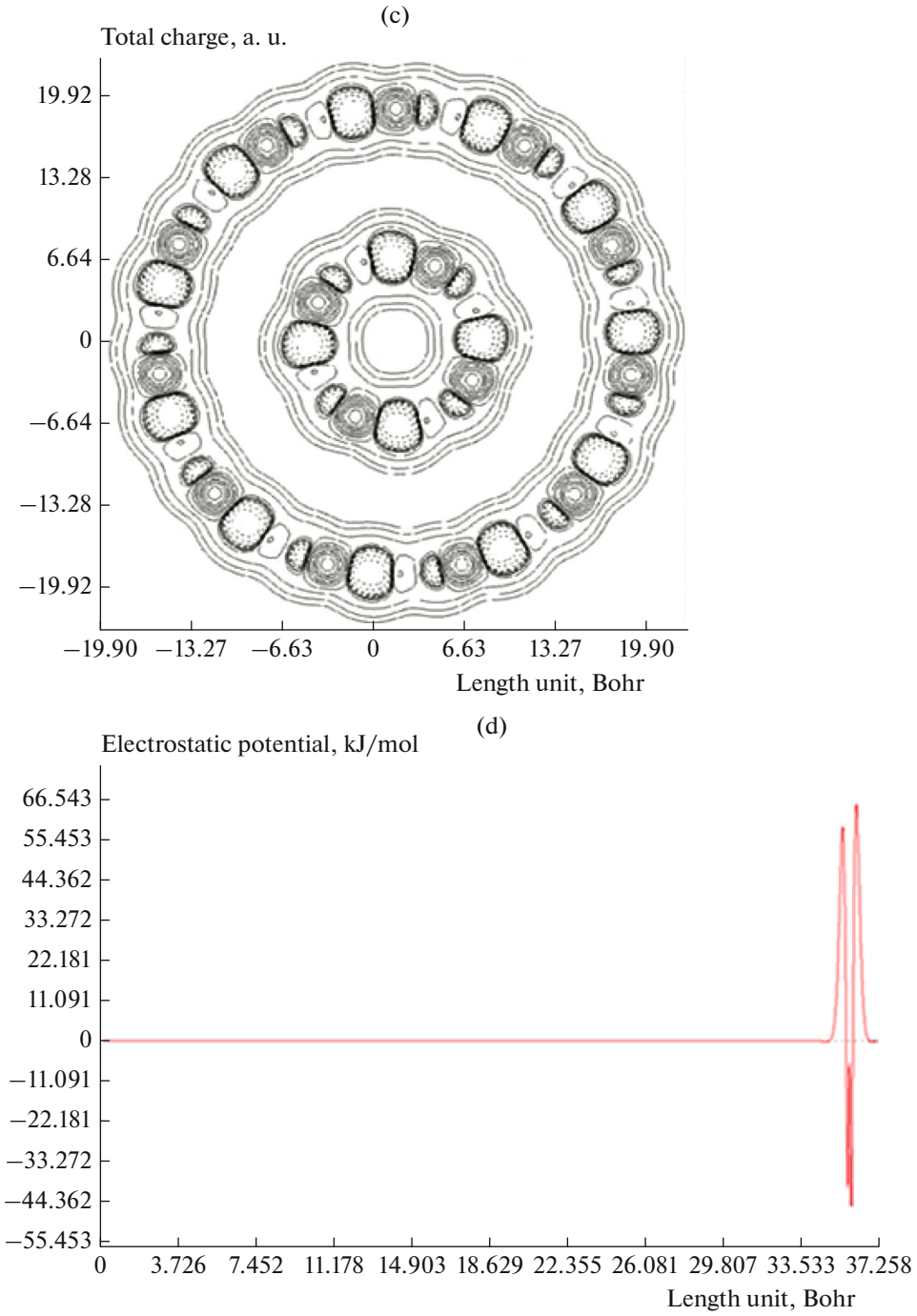

Fig. 9. (Contd.)

strated for the first time. The characteristics of the output voltage have been studied in reference to the numerically calculated piezo-potential, and the mechanism is consistent with that proposed for nanowires. Our conclusion is that ZnO nanotubes can also be applied for harvesting mechanical energy. In addition to the preparation of single-crystalline ZnO nanotubes, we have also demonstrated that a concave shaped crystal growth front is generally reactive and can accommodate more depositing species during rapid expansion of unidirectional nano materials.

FUNDING

This work was supported by ongoing institutional funding. No additional grants to carry out or direct this particular research were obtained.

CONFLICT OF INTEREST

The authors of this work declare that they have no conflicts of interest.

REFERENCES

1. D. Tilman, R. Socolow, J. A. Foley, et al., Science **325**, 270–271 (2009). https://doi.org/10.1126/science.1177970
2. Z. L. Wang and J. Song, Science **312**, 242–246 (2006). https://doi.org/10.1126/science.1124005
3. K. Nomura, H. Ohta, K. Ueda, et al., Science **300**, 1269–1272 (2003). https://doi.org/10.1126/science.1083212
4. S. Xu, Y. Wei, M. Kirkham, et al., J. Am. Chem. Soc. **130**, 14958–14959 (2008). https://doi.org/10.1021/ja806952j
5. B. Weintraub, Y. L. Deng, and Z. L. Wang, J. Phys. Chem. C **111**, 10162–10165 (2007). https://doi.org/10.1021/jp073806v
6. Y. Wei, Y. Ding, C. Li, et al., J. Phys. Chem. C **112**, 18935–18937 (2008). https://doi.org/10.1021/jp807616y
7. Y. Xi, C. G. Hu, X. Y. Han, et al., Solid State Commun. **141**, 506–509 (2007). https://doi.org/10.1016/j.ssc.2006.12.016
8. J. R. Morber, X. Wang, J. Liu, et al., Wang, Adv. Mater. **21**, 2072–2076 (2009). https://doi.org/10.1002/adma.200803648
9. M. H. Huang, S. Mao, H. Feick, et al., Science **292**, 1897–1899 (2001). https://doi.org/10.1126/science.1060367
10. L. Vayssieres, K. Keis, A. Hagfeldt, et al., Chem. Mater. **13**, 4395–4398 (2001). https://doi.org/10.1021/cm011160s
11. V. F. Gromov, M. I. Ikim, G. N. Gerasimov, et al., Russ. J. Phys. Chem. B **15**, 1084–1086 (2021). https://doi.org/10.1134/S1990793121060166
12. Y. Tong, Y. Liu, C. Shao, et al., J. Phys. Chem. B **110**, 14714–14718 (2006). https://doi.org/10.1021/jp056654h
13. J. Q. Hu, Q. Li, X. Meng, et al., Chem. Mater. **15**, 305–308 (2003). https://doi.org/10.1021/cm020649y
14. S.-Y. Yu, H.-J. Zhang, Z.-P. Peng, et al., Inorg. Chem. **46**, 8019–8023 (2007). https://doi.org/10.1021/ic7008978
15. F. Mollaamin and M. Monajjemi, Russ. J. Phys. Chem. B **17**, 658–672 (2023). https://doi.org/10.1134/S1990793123030223
16. Y. Tong, Y. Liu, L. Dong, et al., J. Phys. Chem. B **110**, 20263–20267 (2006). https://doi.org/10.1021/jp063312i
17. E. A. Boruleva, I. A. Nagovitsyn, G. K. Chudinova, et al., Russ. J. Phys. Chem. B **15**, 1087–1094 (2021). https://doi.org/10.1134/S1990793121060026
18. B. P. Zhang, N. T. Binh, K. Wakatsuki, et al., Appl. Phys. Lett. **84**, 4098–4100 (2004). https://doi.org/10.1063/1.1753061
19. F. Mollaamin and M. Monajjemi, Mol. Simul. **49** (4), 365–376 (2023). https://doi.org/10.1080/08927022.2022.2159996
20. J. S. Jeong, J. Y. Lee, J. H. Cho, et al., Chem. Mater. **17**, 2752–2756 (2005). https://doi.org/10.1021/cm049387l
21. S. Bagheri, M. Monajjemi, A. Ziglari, et al., Russ. J. Phys. Chem. B **15** (Suppl. 1), S140–S148 (2021). https://doi.org/10.1134/S1990793121090049
22. C. Pacholski, A. Kornowski, and H. Weller, Angew. Chem. Int. Ed. **41**, 1188–1191 (2002). https://doi.org/10.1002/1521-3773(20020402)41:7
23. F. Mollaamin, S. Shahriari, M. Monajjemi, et al., J. Clust. Sci. **34**, 1547–1562 (2023). https://doi.org/10.1007/s10876-022-02335-1
24. P. X. Gao, Y. Ding, W. Mai, et al., Science **309**, 1700–1704 (2005). https://doi.org/10.1126/science.1116495
25. B. Liu and H. C. Zeng, J. Am. Chem. Soc. **126**, 16744–16746 (2004). https://doi.org/10.1021/ja044825a
26. Z. L. Wang, and J. H. Song, Science **312**, 242–246 (2006). https://doi.org/10.1126/science.1124005
27. A. Wadeasa, O. Nur, and M. Willander, Nanotechnology **20**, 065710 (2009). https://doi.org/10.1088/0957-4484/20/6/065710
28. M. Willander, Y.E. Lozovik, Q. X. Zhao, et al., Proc. SPIE **6486**, 648614 (2007). https://doi.org/10.1117/12.714005
29. M. Riaz, A. Fulati, Q. X. Zhao, et al., Nanotechnology **19**, 415708 (2008). https://doi.org/10.1088/0957-4484/19/41/415708
30. M. Riaz, A. Fulati, L. Yang, et al., J. Appl. Phys. **104**, 104306 (2008). https://doi.org/10.1063/1.3018090
31. J. Liu, C. Guo, C. M. Li, et al., Electrochem. Commun. **11**, 202–205 (2009). https://doi.org/10.1016/j.elecom.2008.11.009
32. O. Lupan, G. Chai, and L. Chow, Microelectron. Eng. **85**, 2220–2225 (2008). https://doi.org/10.1016/j.mee.2008.06.021
33. A. Umar, M. M. Rahman, A. Al-Hajry, et al., Talanta **78**, 284–289 (2009). https://doi.org/10.1016/j.talanta.2008.11.018
34. A. Umar, M. M. Rahman, V. Mohammad. et al., Electrochem. Commun. **11**, 118–121 (2009). https://doi.org/10.1016/j.elecom.2008.10.046
35. A. Umar, M. M. Rahman, and Y.-B. Hahn, J. Nanosci. Nanotechnol. **9**, 4686–4691 (2009). https://doi.org/10.1166/jnn.2009.1103
36. A. Umar, M. M. Rahman, and Y.-B. Hahn, Talanta **77**, 1376–1380 (2009). https://doi.org/10.1016/j.talanta.2008.09.020
37. A. Umar, M. M. Rahman, S. H. Kim, et al., Chem. Commun. **2**, 166–168 (2008). https://doi.org/10.1039/B711215G
38. X. D. Bai, P. X. Gao, Z. L. Wang, et al., Appl. Phys. Lett. **82**, 4806–4808 (2003). https://doi.org/10.1063/1.1587878

39. Z. L. Wang and J. H. Song, Science **312**, 242–246 (2007). https://doi.org/10.1126/science.1124005

40. Q. X. Zhao, P. Klason, M. Willander, et al., Phys. Scr. **126**, 131–134 (2006). https://doi.org/10.1088/0031-8949/2006/T126/029

41. L. Oleg, C. Lee, C. Guangyu, et al., Mater. Sci. Eng. B **145**, 57–66 (2007). https://doi.org/10.1016/j.mseb.2007.10.004

42. Q. X. Zhao, P. Klason, and M. Willander, Appl. Phys. A: Mater. Sci. Process. **88**, 27–30 (2007). . https://doi.org/10.1007/s00339-007-3958-0

43. K. Kitamura, T. Yatsui, M. Ohtsu, Appl. Phys. Express **1**, 081202 (2008). https://doi.org/10.1143/APEX.1.081202

44. A. Fulati, S. M. Usman Ali, M. Riaz, et al., Sensors **9**, 8911–8923 (2009). https://doi.org/10.3390/s91108911

45. Y. Xi, J. Song, S. Xu, et al., J. Mater. Chem. **19**, 9260–9264 (2009). . https://doi.org/10.1039/B917525C

46. T. Kamiya and M. Kawasaki, MRS Bull. **33**, 1061–1066 (2008). https://doi.org/10.1557/mrs2008.226

47. H. Guo, J. Zhou and Z. Lin, Electrochem. Commun. **10**, 146–150 (2008). https://doi.org/10.1016/j.elecom.2007.11.010

48. Z. L. Wang, Adv. Funct. Mater. **18**, 3553–3567 (2008). https://doi.org/10.1002/adfm.200800541

49. J. Song, J. Zhou and Z. L. Wang, Nano Lett. **6**, 1656–1662 (2006). https://doi.org/10.1021/nl060820v

50. S. Iijima and T. Ichihashi, Nature **363**, 603–605 (1993). https://doi.org/10.1038/363603a0

51. G. Bilalbegovic, Phys. Rev. B **58**, 15412 (1998). https://doi.org/10.1103/PhysRevB.58.15412

52. G. Bilalbegovic, Solid State Commun. **115**, 73–76 (2000). https://doi.org/10.1016/S0038-1098(00)00149-6

53. G. Bilalbegovic, Comput. Mater. Sci. **18**, 333–338 (2000). https://doi.org/10.1016/S0927-0256(00)00113-0

54. I. S. Gradshteyn and I. M. Ryzhik, *Table of Integrals, Series, and Products* (Academic Press, New York, 1965).

55. W. A. de Heer, Rev. Mod. Phys. **65**, 611–615 (1993). https://doi.org/10.1103/RevModPhys.65.611

56. S. Wang and M. Grifoni, Phys. Rev. B **77**, 085431 (2008). https://doi.org/10.1103/PhysRevB.77.085431

57. T. Lu and F. Chen, Acta Chim. Sinica **69**, 2393–2406 (2011).

58. T. Lu and F. Chen, J. Mol. Graph. Model. **38**, 314–323 (2012). https://doi.org/10.1016/j.jmgm.2012.07.004

59. Tian Lu, Feiwu Chen, J. Comp. Chem. **33**, 580–592 (2012). https://doi.org/10.1002/jcc.22885

60. M. W. Schmidt, K. K. Baldridge, J. A. Boatz, et al., J. Comput. Chem. **14**, 1347–1363 (2004). https://doi.org/10.1002/jcc.540141112

61. Y. Zhao, D. G. Truhlar, Theor. Chem. Account **119**, 525 (2008). https://doi.org/10.1007/s00214-007-0401-8

62. W. Kohn and L. J. Sham, Phys. Rev. **140**, A1133–A1138 (1965). https://doi.org/10.1103/PhysRev.140.A1133

63. J. P. Perdew, K. Burke, M. Ernzerhof, Phys. Rev. Lett. **77**, 3865–3868 (1996). https://doi.org/10.1103/PhysRevLett.77.3865

64. D. L. Klein, R. Roth, A. K. L. Lim, et al., Nature **389**, 699-701 (1997). https://doi.org/10.1038/39535

65. Y. Zhao and D. G. Truhlar, Acc. Chem. Res. **41** (2), 157–167 (2008). https://doi.org/10.1021/ar700111a

66. C. E. Check and T. M. Gilbert, J. Org. Chem. **70**, 9828–9834 (2005). https://doi.org/10.1021/jo051545k

67. S. Grimme, Angew. Chem., Int. Ed. **45** 4460–4464 (2006). https://doi.org/10.1002/anie.200600448

68. B. H. Besler, K. M. Merz Jr., P. A. Kollman, J. Comp. Chem. **11**, 431–439 (1990). https://doi.org/10.1002/jcc.540110404

69. L. E. Chirlian and M. M. Francl, J. Comp. Chem. **8**, 894–905 (1987). https://doi.org/10.1002/jcc.540080616

70. G. M. Brneman and K. B. Wiberg, Comp. Chem. **11**, 361–373 (1990). https://doi.org/10.1002/jcc.540110311

71. F. Martin and H. Zipse, J. Comp. Chem. **26**, 97–105 (2005). https://doi.org/10.1002/jcc.20157

72. M. Monajjemi, V. S. Lee, M. Khaleghian, et al., J. Phys. Chem. C **114**, 15315–15330 (2010). https://doi.org/10.1021/jp104274z

73. M. Monajjemi, and M. Khaleghian, J. Clust. Sci. **22**, 673–692 (2011). https://doi.org/10.1007/s10876-011-0414-2

74. M. Monajjemi, Struct. Chem. **23**, 551–580 (2012). https://doi.org/10.1007/s11224-011-9895-8

75. H. Chou and H. Z. Cummins, Phys. Rev. Lett. **61**, 173 (1988). https://doi.org/10.1103/PhysRevLett.61.173